THE JOURNAL OF PHYSICAL CHEMISTRY Letters

pubs.acs.org/JPCL Letter

Organic Cations Protect Methylammonium Lead Iodide Perovskites against Small Exciton-Polaron Formation

Guangjun Nan,* David Beljonne, Xu Zhang, and Claudio Quarti

Cite This: J. Phys. Chem. Lett. 2020, 11, 2983−2991 Read Online

ACCESS | Metrics & More | Article Recommendations | Supporting Information

ABSTRACT: Working organic−inorganic lead halide perovskite-based devices are notoriously sensitive to surface and interface effects. Using a combination of density functional theory (DFT) and time-dependent DFT methods, we report a comprehensive study of the changes (with respect to the bulk) in geometric and electronic structures going on at the (001) surface of a (tetragonal phase) methylammonium lead iodide perovskite slab, in the dark and upon photoexcitation. The formation of a hydrogen bonding pattern between the -NH_3 groups of the organic cations and the iodine atoms of the outer inorganic layout is found to critically contribute to the relative thermodynamic stability of slabs with varying surface compositions and terminations. Most importantly, our results show that the hydrogen bond locking effects induced by the MA groups tend to protect the external two-dimensional lattice against large local structural deformations, i.e., the formation of a small exciton-polaron, at variance with purely inorganic lead halide perovskites.

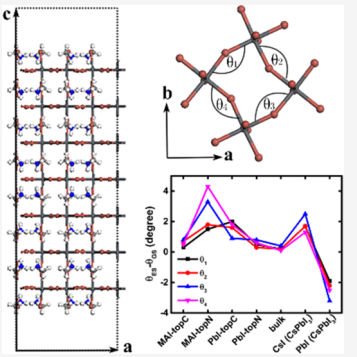

Hybrid organic−inorganic halide perovskites, such as $MAPbI_3$ (MA = CH_3NH_3), are being more heavily scrutinized due to their outstanding optoelectronic properties.[1] Namely, over the past few years, the power conversion efficiencies of lead halide-based perovskite solar cells have increased rapidly.[2] The impressive photovoltaic performances demonstrated by this class of materials are triggered by a combination of several unique features, including a wide optical absorption range,[3] a large optical absorption coefficient,[4] and a long charge carrier diffusion length.[5] In particular, low electron-hole (e-h) binding energies of <20 meV have been widely reported.[6−11] As the value of the e-h binding energy is smaller than kT (~25 meV) at room temperature, it is reasonable to expect that most of the weakly bound e-h pairs are ionized, yielding free carriers in the bulk.[12−14]

Tracking the initial charge carrier dynamics following photoexcitation using transient spectroscopy provides useful information about the possible coupling between the electronic and nuclear degrees of freedom.[15] While literature data abundantly refer to the formation of self-trapped excitons[16,17] or photoinduced polarons[18−20] in lead halide perovskites, their detailed nature in relation to chemical composition and dimensionality has not been clearly unveiled.[21] Using the common language in the field, "large" polarons,[22,23] i.e., extended lattice distortions responsible for the appearance of shallow energy traps in the band gap, can form in $MAPbI_3$ as a result of the reorientation of the dipolar organic cations and their associated screening fields,[24] distortions in the inorganic framework on subpicosecond time scales[25,26] (thus being much faster than the rotation of the organic cations),[27] or a combination of both displaced inorganic nuclei and reoriented organic cations.[28] In addition to large polarons in the three-dimensional (3D) bulk, a number of theoretical and experimental investigations also suggest the formation of "small" polarons, i.e., a localized reorganization of the lattice pushing energy levels deep in the band structure.[29,30] While large polarons are expected to have a rather benign impact on charge transport and recombination, small (exciton) polarons feed the formation of (transient, if these are triggered by light absorption) deep traps that can reduce charge carrier mobility and enhance trap-assisted recombination at low charge carrier densities. We note that, because of electronic and dielectric confinement effects, low-dimensional perovskites are expected to undergo enhanced carrier-phonon interactions, possibly prompting the formation of small polarons.[31] It is also likely that larger structural reorganization in charged or neutral excited states occurs close to perovskite surfaces as these offer increased ion mobility.[32,33]

Theoretical calculations have been performed to assess at the atomistic level the fundamental (photo)physics of perovskite surfaces, such as the thermodynamic stability of different terminations[34−36] and the associated changes in the ground-state electronic structure[37−39] or the degradation mechanisms in contact with the atmosphere or moisture.[38,40−45] While there is clear evidence for substantial

Received: March 2, 2020
Accepted: March 30, 2020
Published: March 30, 2020

https://dx.doi.org/10.1021/acs.jpclett.0c00673
J. Phys. Chem. Lett. 2020, 11, 2983−2991

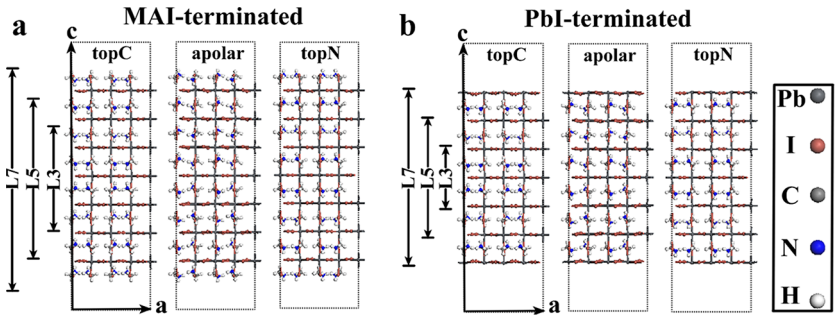

Figure 1. (a) $MAPbI_3$ with MAI-terminated surfaces. (b) $MAPbI_3$ with PbI-terminated surfaces. The topC, apolar, and topN configurations defined in the text are shown for each surface termination. The thickness of the slabs is defined as L*n* (*n* = 3, 5, or 7), where *n* is the number of the PbI_2 planes along the *c* axis.

surface reconstruction effects,[46−48] how these ground-state effects in turn translate into local lattice distortions upon light irradiation, i.e., after formation of e-h pairs, has remained largely unexplored.[49]

This is precisely the scope of this work, in which we apply state-of-the-art density functional theory (DFT) and time-dependent DFT (TD-DFT) techniques to track the energetics of neutral excitations in slab models of $MAPbI_3$ upon relaxing the ionic forces in the excited state. We find that exciton-polaron relaxation energies anticorrelate with the thermodynamic stability of the ground-state surface (namely, more stable surfaces show smaller relaxation energies), hence pointing to the important role played by hydrogen bonding between the amino groups and the iodines in protecting the semiconducting material against the formation of deep trap states.

We focus on the (001) surface of $MAPbI_3$ in the tetragonal phase owing to the high surface stability predicted by both first-principles calculations[35,50] and powder X-ray diffraction measurements.[51] Two typical surface terminations are studied:[37,38] MAI termination that exposes MA cations and iodine atoms (Figure 1a) and PbI termination that exposes lead and iodine atoms (Figure 1b). Fixing the cell parameters of the tetragonal phase ($a = b = 8.8556$ Å) at their room-temperature values obtained by Poglitsch and Weber,[52] we construct the slabs by considering a 2 × 2 periodicity in the *a*−*b* plane (Figure 1). The thickness of the slabs is defined as the number of PbI_2 layers (L*n*) along the direction normal to the *a*−*b* plane. Slabs of increasing thicknesses (L*n*, where *n* = 3, 5, or 7) were compared to a bulk model (using a 2 × 2 × 2 supercell that has been shown to provide a reasonable description of the band gap).[4,53] To eliminate the spurious interactions between the slabs and their periodic images along the *c* axis, a distance of 65 Å in the normal direction of the surfaces is adopted (corresponding to a vacuum region of at least 18 Å). Note that each of the studied slabs is symmetric with respect to the innermost PbI_2 plane to avoid artifacts associated with the formation of a polar slab.[37] Because the frontier crystal orbitals are controlled by the orientation of the MA cations,[37] three models are studied for each of the terminated surfaces. (i) In the topC model, the MA cations have their C-terminated sides oriented toward the vacuum. (ii) In the topN model, the MA cations are oriented with their N-terminated sides pointing to the vacuum. (iii) In the apolar model, the MA cations show alternated orientations in each *a*−*b* plane (namely, half of the MA cations with their N-terminated sides pointing up and half pointing down).

The ground-state calculations are carried out by using the DFT method under periodic boundary conditions, as implemented in the Vienna Ab initio Simulation Package.[54] The electronic wave functions are expanded by plane waves with an energy cutoff of 400 eV. Atoms of Pb, I, C, N, and H species are explicitly treated by incorporating 14, 7, 4, 5, and 1 valence electrons, respectively. The structural relaxations are performed with projector-augmented wave pseudopotentials[55] and the Perdew−Burke−Ernzerhof (PBE) functional[56] by sampling the Brillouin zone at the Γ point. The energy convergence criterion is set to 10^{-4} eV, and the positions of all atoms are relaxed until the Hellman−Feynman forces become smaller than 0.04 eV/Å. The semiempirical DFT-D_2 method is used to account for the van der Waals corrections,[57] potentially affecting the interaction between the MA cation and the inorganic lattice.[37] On the basis of the DFT fully optimized ground-state configurations, relaxation of the ionic forces in the excited state is performed by applying a recently developed TD-DFT approach using pseudopotentials and a plane wave basis set, suitable for calculations on periodic systems.[58] The ionic forces and charge densities in the excited states are obtained by the derivatives of the Lagrangian functional with respect to ionic position and external potential, respectively. From the literature, it is well-established that the PBE functional produces reasonable values for the band gap of hybrid perovskites due to a cancellation of two effects, namely, the lack of spin−orbital interactions and the self-interaction error inherent to pure DFT functionals.[59−61] To validate the PBE results, calculations including spin−orbit coupling (SOC) corrections and applying an optimally tuned range-separated hybrid (OT-RSH) functional[62] have also been carried out. Because of the large size of the models with which we are dealing, we resort to solving the OT-RSH functional problem using first-order perturbation theory,[63,64] which has been shown to produce reasonable optical excitations in solids with dielectric confinement effects.[65]

MAI-terminated slabs with topC, apolar, and topN configurations are hereafter defined as MAI-topC, MAI-apolar, and MAI-topN, respectively. Similarly, the PbI-terminated slabs with topC, apolar, and topN configurations are labeled PbI-topC, PbI-apolar, and PbI-topN, respectively. When comparing the relative total ground-state energies of the slabs, we find that the topC (topN) configuration is the most (least) stable for MAI-terminated slabs (Figure 2a). The relative stabilities are swapped for PbI-terminated slabs, with now the topN (topC) configuration becoming the most (least) stable (Figure 2b). Such trends hold irrespective of the thickness of the slabs (Figure S1), suggesting that the relative

https://dx.doi.org/10.1021/acs.jpclett.0c00673
J. Phys. Chem. Lett. 2020, 11, 2983−2991

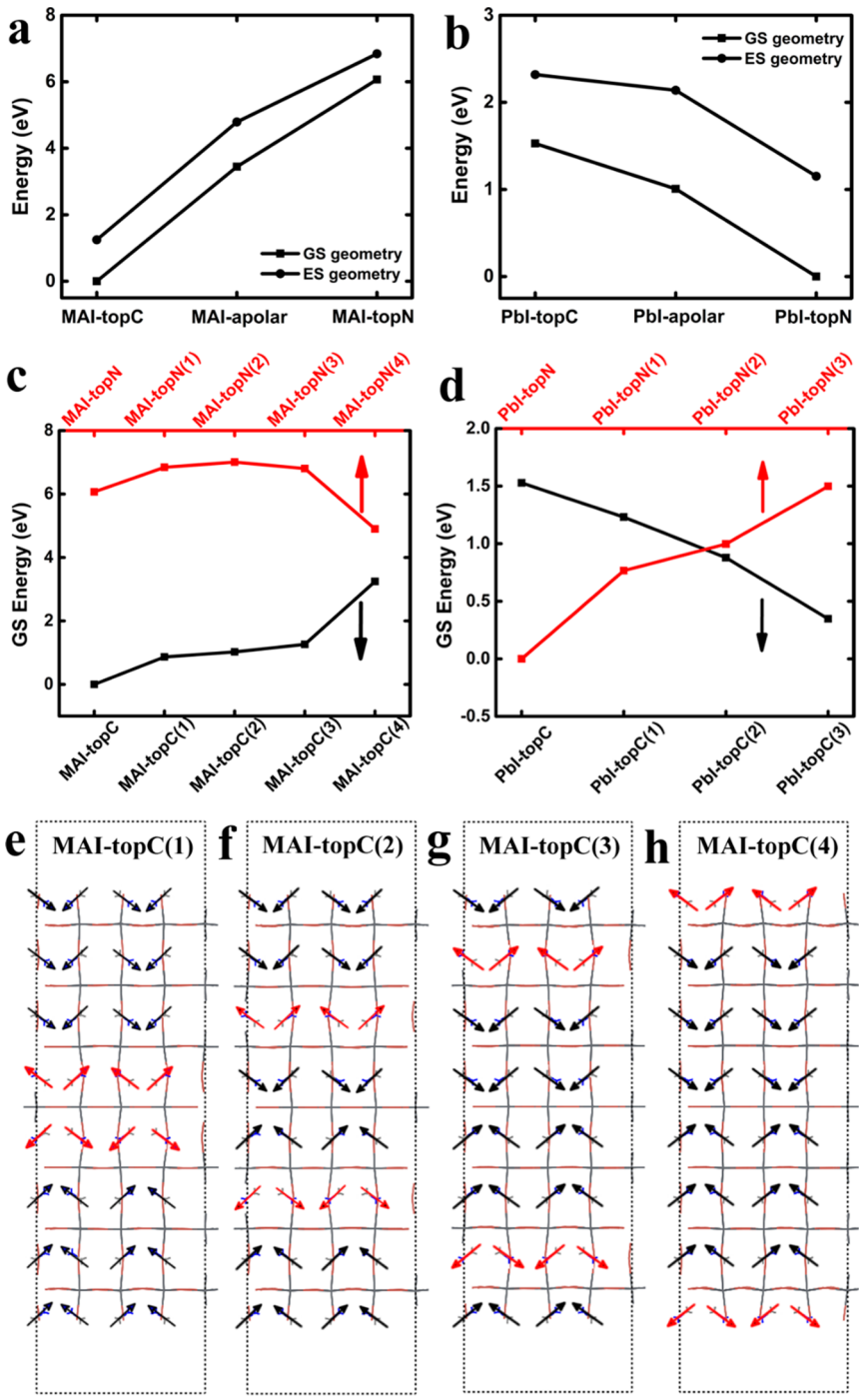

Figure 2. Energetics of L7 slabs as a function of the orientation of the dipolar MA cations. (a) Ground-state (GS) and excited-state (ES) energies for the MAI-topC, MAI-apolar, and MAI-topN slabs in the relaxed GS and ES geometry, respectively. (b) GS and ES energies for the PbI-topC, PbI-apolar, and PbI-topN slabs in the relaxed GS and ES geometry, respectively. (c) GS energies of MAI-terminated slabs in topC and topN configurations with reversed MA cations in different $a-b$ planes. (d) GS energies of PbI-terminated slabs in topC and topN configurations with reversed MA cations in different $a-b$ planes. The energies in panels a and c are taken with respect to the GS energies of the MAI-topC slab, whereas the energies in panels b and d are taken with respect to the GS energies of the PbI-topN slab. (e–h) Configurations of MAI-topC(n) (n = 1, 2, 3, and 4, respectively) that are defined as the MAI-topC slab with the reversed MA cations (red) in the nth layers counting from the innermost PbI_2 plane. The configurations of MAI-topN(n) in panel c correspond to the MAI-topN slab with reversed MA cations in the nth layers counting from the innermost PbI_2 plane. PbI-topC(n) and PbI-topN(n) (n = 1, 2, and 3) in panel d are defined in the same way as MAI-topC(n) and MAI-topN(n).

stability of the slabs is influenced by an interplay between the orientation of the organic cations and the surface exposure. To gain more insight into this, we performed calculations by successively rotating MA cations in different $a-b$ planes (Figure 2e–h). Focusing on the MAI-terminated surface, we find that (i) among the MAI-topC slabs, the rotation of the outermost cationic layer with -NH_3 moieties pointing toward the vacuum, the MAI-topC(4) model, results in the largest

https://dx.doi.org/10.1021/acs.jpclett.0c00673
J. Phys. Chem. Lett. 2020, 11, 2983–2991

energy destabilization (~3 eV per slab), while the other rotations account for a smaller destabilization [~1.5 eV (Figure 2c)], and (ii) among the MAI-topN slabs, the rotation of the outermost cationic layer with -NH_3 moieties pointing toward the bulk, MAI-topN(4) model, results in the largest energy stabilization (~1.6 eV), while all of the other rotations slightly destabilize the system. The surface topology of $MAPbX_3$ (X = I or Br) has been resolved in real space experimentally using scanning tunneling experiments,[46,47] showing the final surface structure with MAX termination and the external CH_3 groups directed toward vacuum, hence essentially in line with the MAI-topC model reported here.

The increased stability in MAI-terminated surfaces where the top layer MA cations orient their -NH_3 units toward the bulk (-CH_3 toward vacuum) has to be ascribed to the formation of hydrogen bonds (HBs) with the halides,[42] as confirmed by the calculations presented here. More specifically, using a cutoff criterion of ≤3 Å for the H···I distance, we find that the MAI-topC and MAI-topN(4) models are characterized by four HBs per organic cation on the surfaces (Figure 3a and Table 1), while MAI-topC(4) and MAI-topN show only two HBs (Figure 3b and Table 1). The energy penalty to switch one outermost MA cation [from MAI-topC to MAI-topC(4), consequently breaking two HBs] is hence estimated to be ~200 meV per cation, translating into a hydrogen bonding energy of ~100 meV, in good agreement with earlier theoretical calculations[66] and with typical values reported for H···I interactions.[67] In summary, the breaking of the hydrogen bonding network between the organic cations and the PbI lattices at the perovskite surface explains the destabilization of the MAI-topN and MAI-topC(4) models, compared to MAI-topC. When focusing on the PbI-terminated surfaces, we find the PbI-topN slab is stabilized by the formation of four HBs for each MA cation, two with the outermost iodine atoms and two with iodine atoms residing in the bulk (Figure 3d and Table 1). Upon rotation of the outermost MA cations, model PbI-topN(3) (Figure 3c), the hydrogen bonds with external iodines are broken and substituted with two new HBs inside the bulk, leading to the smaller energy variation (~40 meV), compared to that of the models with MAI termination. Taken together, our results confirm previous investigations that highlight the importance of hydrogen bonding in stabilizing the surface of $MAPbI_3$ and suggest that unbalanced HB interactions in the bulk and at surfaces or interfaces might seed surface reconstruction effects.[68]

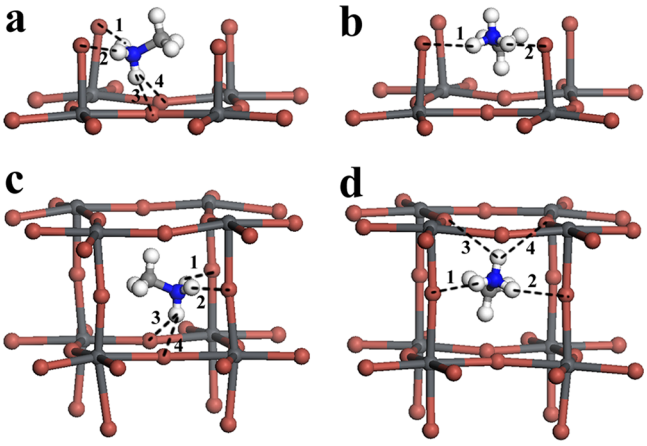

Figure 3. (a and b) Geometry of the MAI-terminated surface with the outermost -CH_3 and -NH_3 groups oriented toward vacuum, respectively. (c and d) Geometry of the PbI-terminated surface with the outermost -CH_3 and -NH_3 moieties oriented toward the surface, respectively. The hydrogen bonds with I···H distances of ≤3 Å are numbered.

We now turn to excited-state properties, here modeled using the TD-DFT approach. The slab models described above have been subjected to full relaxation of the ionic forces in their lowest electronic excited state. Similarly, a 2 × 2 × 2 supercell of the tetragonal phase of $MAPbI_3$, taken as a reference of the 3D bulk material, has been relaxed as well in the lowest excited state. The corresponding adiabatic excited-state energies, plotted versus surface termination in panels a and b of Figure 2, parallel the ground-state energies and reflect changes in HB interactions in the uttermost layer. To quantify the magnitude of the light-triggered geometric changes, we report in Figure 4 the polaronic energy (E_{pol}), defined as the difference in excitation energies between the equilibrium geometries in the ground state and excited state. Notably, compared to the corresponding 3D bulk, a similar increase in polaronic reorganization energies has been reported by Neukirch et al. in model clusters of $MAPbI_3$.[30] The reorganization energy increases significantly from L3 to L5, with some sign of saturation at L7, thus implying that the intrinsic size of "surface" polarons in $MAPbI_3$ extends over a thickness of at least two PbI_6 octahedra. Interestingly, irrespective of the thickness of the slabs, the MAI-topC samples, which are also

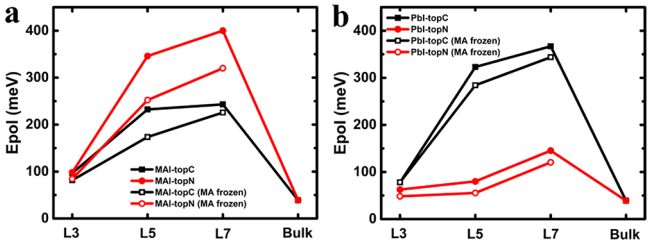

Figure 4. Polaronic energies (E_{pol}) as a function of the thickness of the slabs: (a) MAI-topC and MAI-topN slabs and (b) PbI-topC and PbI-topN slabs. The data shown as filled symbols are obtained by fully relaxing the excited-state geometries, whereas the data shown as empty symbols are obtained by freezing the MA cations during the excited-state relaxation. The E_{pol} of the $MAPbI_3$ bulk with a 2 × 2 × 2 supercell is also shown in panels a and b.

Table 1. Distances (angstroms) of the HBs Formed between -NH_3 Groups and Iodine Atoms Shown in Figure 3

	MAI-topC	MAI-topN	MAI-topC(4)	MAI-topN(4)	PbI-topC	PbI-topN	PbI-topC(3)	PbI-topN(3)
1	2.57	2.58	2.81	2.77	2.68	2.71	2.88	2.83
2	2.61	2.53	2.85	2.73	2.73	2.77	2.87	2.96
3	2.94			3.00	3.00	3.00	3.00	2.96
4	2.96			2.82	2.99	2.86	3.00	2.98

https://dx.doi.org/10.1021/acs.jpclett.0c00673
J. Phys. Chem. Lett. 2020, 11, 2983−2991

the most stable, display smaller E_{pol} values compared to those of MAI-topN (Figure 4a), the same being true for the PbI-topN versus PbI-topC slabs (Figure 4b). Thus, there is a clear anticorrelation between ground-state stability and geometric relaxation as measured by the polaron relaxation energy in these slabs, with most stable surfaces showing smaller relaxation energies. It is instructive to further disentangle the polaronic effects into contributions from the inorganic and organic components. This is modeled here by freezing the MA cations during the excited-state optimization, thus removing the contribution to the polaronic relaxation associated with the organic component. From this analysis (Figure 4), we conclude that the lattice distortions are contributed by both collective motions of the inorganic lattice and (though to a smaller extent) reorientation of the organic cations, in line with theoretical calculations[29,30] and experimental studies.[28,69]

To gauge the effects of such geometric deformations on the electronic structure, we proceed to analyze the one-electron density of states (DOS) along the surface normal at both the ground-state and excited-state equilibrium geometries, as depicted in Figures 5 and 6. The thickest (L7) MAI- and

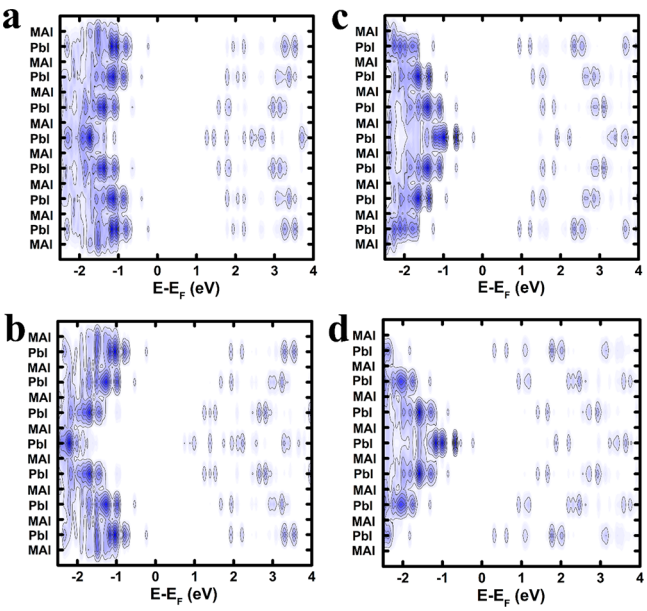

Figure 5. Surface plot of the DOS for the L7 slabs with MAI termination. (a) DOS of the MAI-topC slab in the ground state. (b) DOS of the MAI-topC slab in the excited state. (c) DOS of the MAI-topN slab in the ground state. (d) DOS of the MAI-topN slab in the excited state.

PbI-terminated slabs are used for this analysis. The spatial confinement of the crystalline orbitals when moving away from the surface to the bulk reflects changes in electrostatics, with the valence and conduction edge states bending in real space as a function of the orientation of the MA cations, which lies parallel to the polarization of the material.[70] Specifically, when we focus on the ground-state results, the DOS distribution calculated for MAI-topC shows a "<" like shape for both the valence and conduction band states, indicating that holes are stabilized at the outer layers while the electrons are confined in the central layers; this pattern reflects the orientation of the MA dipoles that point their negative (positive) heads toward (backward) vacuum thereby shifting the hole (electron) density outward (inward). In fact, in the MAI-topN

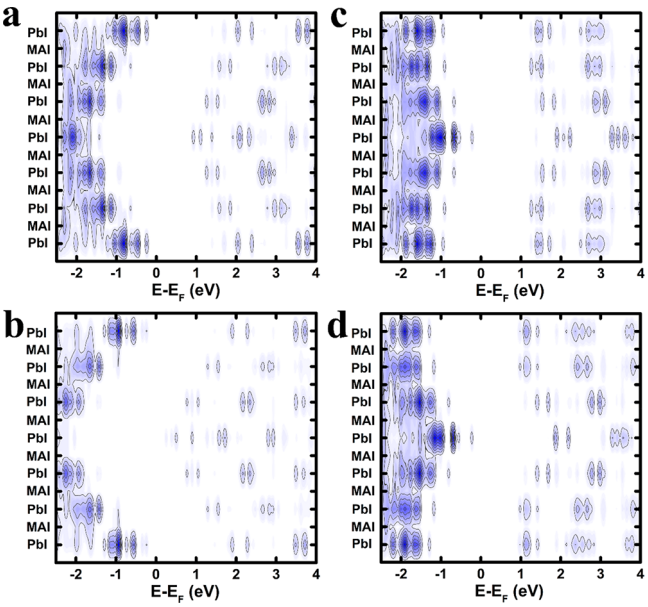

Figure 6. Surface plot of the DOS for the L7 slabs with PbI termination. (a) DOS of the PbI-topC slab in the ground state. (b) DOS of the PbI-topC slab in the excited state. (c) DOS of the PbI-topN slab in the ground state. (d) DOS of the PbI-topN slab in the excited state.

configuration, the surface electrostatic potential is inverted, and so is the DOS now featuring a ">" shape with the conduction (valence) band confined in the outer (inner) layers. Thus, there is an intrinsic driving force for spatially splitting holes and electrons apart in these slabs that arises from surface dipole effects. These effects, already present in panels a and c of Figure 5 pertaining to the ground-state geometries, are apparently amplified upon geometric relaxation in the excited state (Figure 5b,d). Very similar results are obtained for the PbI-terminated surfaces (see Figure 6). We have also verified that the surface dipole effects driving spatial separation of holes and electrons are present in the slabs with an overall apolar bulk configuration (Figure S2).

The changes in DOS occurring in the excited-state equilibrium geometry can be mostly related to distortions of the octahedral lattice (though changes in the orientation of the organic cations also contribute). Figure 7b shows that there is a substantial and rather uniform deformation of the lattice in the outermost PbI_2 plane that tends to straighten the Pb−I−Pb linkages, prompting an increased level of Pb−I hybridization, while alternating increases and decreases in bond angles occur in the deeper layers (Figure 7c,d). Most importantly, such structural reorganization effects are strongly suppressed when going from the less stable MAI-topN and (to a lesser extent) PbI-topC to the thermodynamically favored MAI-topC and PbI-topN slabs, which explains the reduced polaronic energies of the latter. It thus appears that hydrogen bonding interactions that are responsible for the increased stability of the latter two configurations also protect the surfaces against the formation of strongly bound exciton-polarons. Notably, PbI-terminated surfaces show weaker geometric deformation than MAI-terminated surfaces when going from the ground state to the excited state. Though other effects could contribute, this seems to correlate with the improved performance of $MAPbI_3$-based solar cells with PbI-terminated exposure.[71−73]

https://dx.doi.org/10.1021/acs.jpclett.0c00673
J. Phys. Chem. Lett. 2020, 11, 2983−2991

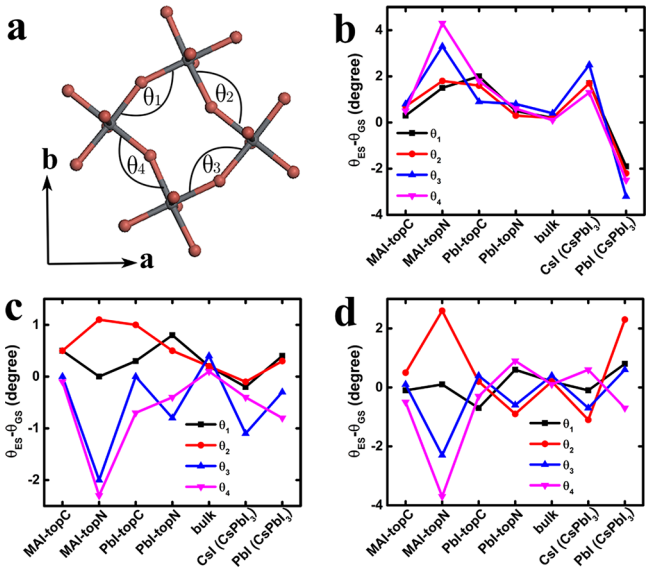

Figure 7. (a) Pb−I−Pb angles in the equatorial PbI_2 planes are defined. (b) Changes in angles in the outermost PbI_2 plane from the GS geometry to the ES geometry. (c) Changes in angles in the second outermost PbI_2 plane from the GS geometry to the ES geometry. (d) Changes in angles in the third outermost PbI_2 plane from the GS geometry to the ES geometry. CsI($CsPbI_3$) and PbI($CsPbI_3$) in panels b−d represent the CsI- and PbI-terminated $CsPbI_3$ slabs, respectively.

To further corroborate these findings, we performed similar calculations replacing all MA cations with cesium ions (while maintaining the $MAPbI_3$ tetragonal lattice structure for ease of comparison). In line with our hypothesis, the lack of HB interactions in $CsPbI_3$ results in large-amplitude angle deformations in the outermost PbI_2 plane and in associated large polaron relaxation energies (320 meV for CsI-terminated $CsPbI_3$ and 250 meV for PbI-terminated $CsPbI_3$). The difference with respect to the polaron energies of the reference MAI-topC and PbI-topN models in Figure 4 (240 and 150 meV, respectively) is therefore purely associated with the HBs. Notably, the large deformation on the surface of $CsPbI_3$ is consistent with the strong carrier-phonon coupling resolved experimentally.[74−80]

Finally, we comment on two aspects that have not yet been addressed. The first is methodological, and the second deals with the importance of e-h correlation effects. All calculations so far are based on the PBE functional. We have verified that the findings described above are (qualitatively) not affected by including SOC corrections (Figure S3) and by properly treating long-range e-h interaction effects using the OT-RSH functional [thinner slabs were adopted due to the large computational cost (Figure S4)]. Because SOC has a rather limited effect on polaronic reorganization energies[81] and under the reasonable hypothesis that corrections to the total energies going beyond pure DFT exchange and correlation should be similar in the ground state and in the excited state, we expect the trends in Figure 4 to be preserved at the hybrid+SOC level of theory.

Notably, reasonable band gap values were obtained by assuming a static dielectric constant of ∼4 (Figure S5), suggesting weaker electrostatic screening at the surface than in the bulk.[82] To shed light on the role of e-h interactions, we repeated our calculations for charged supercells in which geometric relaxation effects were monitored after adding (subtracting) one unit of electron charge to (from) the slabs. The PBE results show that the deformation of the outermost inorganic lattice in the charged state (Figure S6) is substantially weaker than in the neutral excited state turning into exciton-polaron relaxation energies substantially larger than the sum of the hole and electron polaronic energies (Table S1). These results suggest the e-h interactions have a significant impact on the nature of the photoinduced excitations at perovskite surfaces and should thus be accounted for when modeling interfacial light-induced degradation.[83]

To summarize, we have performed DFT and TD-DFT calculations on periodic slabs of MAI- and PbI-terminated $MAPbI_3$ surfaces differing in chemical composition and terminations. Our results are as follows. (i) The thermodynamic stability of the surfaces is found to be critically determined by the orientation of the MA cations. Irrespective of the surface composition, the hydrogen bonding pattern between the $-NH_3$ moieties and the outer iodine atoms steers the relative stability of the slabs in their ground-state and excited-state geometries. (ii) While exciton-polarons have very small binding energies in the bulk, they are stabilized by larger lattice reorganization at surfaces. Yes, these distortions are inversely proportional to the stability of the slabs, with the HB-driven most stable surface models being subjected to the smallest geometric relaxation effects. Hence, it appears that the formation of the HB pattern protects $MAPbI_3$ perovskite surfaces against formation of light-triggered small exciton-polarons and deep photoinduced traps. In fact, simulations performed in corresponding models for $CsPbI_3$ perovskites, where such a HB pattern is absent, show large excitonic relaxation effects. (iii) Compared to the bulk, the surfaces show weaker electrostatic screening of the photogenerated e-h pairs. In turn, the strengthened e-h interactions yield larger structural deformations at surfaces and should be accounted for when theoretically modeling photoinduced processes at surfaces of (interfaces with) $MAPbI_3$.

Our results provide an unambiguous link between the microscopic surface structures and light-induced geometric deformation of $MAPbI_3$ with different surface exposures, and pave the way toward unveiling the photoinduced instability of surfaces in contact with atmospheric species and moisture.[68]

■ ASSOCIATED CONTENT

Supporting Information

The Supporting Information is available free of charge at https://pubs.acs.org/doi/10.1021/acs.jpclett.0c00673.

Energetics and DOS of slabs, polaronic energies and excitation energies as well as charge densities of slabs calculated by the TD-DFT approach with PBE and OT-RSH functionals, and deformation of the inorganic lattice from the neutral state to charged states (PDF)

■ AUTHOR INFORMATION

Corresponding Author

Guangjun Nan − *Department of Physics, Zhejiang Normal University, Jinhua, Zhejiang 321004, P. R. China;* orcid.org/0000-0002-5185-8336; Email: gjnan@zjnu.edu.cn

https://dx.doi.org/10.1021/acs.jpclett.0c00673
J. Phys. Chem. Lett. 2020, 11, 2983−2991

Authors

David Beljonne − *Laboratory for Chemistry of Novel Materials, University of Mons, B-7000 Mons, Belgium;* orcid.org/0000-0002-2989-3557

Xu Zhang − *Department of Physics and Astronomy, California State University Northridge, Northridge, California 91330-8268, United States;* orcid.org/0000-0002-6491-3234

Claudio Quarti − *Laboratory for Chemistry of Novel Materials, University of Mons, B-7000 Mons, Belgium;* orcid.org/0000-0002-5488-1216

Complete contact information is available at: https://pubs.acs.org/10.1021/acs.jpclett.0c00673

Notes

The authors declare no competing financial interest.

■ ACKNOWLEDGMENTS

G.N. acknowledges the support by the Zhejiang Provincial Natural Science Foundation of China (LY20A040003). Research in Mons is supported by FNRS-FRFC and Consortium des Equipements de Calcul Intensif (CECI). C.Q. is a postdoctoral researcher, and D.B. is the research director of FNRS.

■ REFERENCES

(1) Manser, J. S.; Christians, J. A.; Kamat, P. V. Intriguing Optoelectronic Properties of Metal Halide Perovskites. *Chem. Rev.* **2016**, *116*, 12956−13008.

(2) Li, Z.; Klein, T. R.; Kim, D. H.; Yang, M.; Berry, J. J.; van Hest, M. F. A. M.; Zhu, K. Scalable Fabrication of Perovskite Solar Cells. *Nat. Rev. Mater.* **2018**, *3*, 18017.

(3) Saliba, M.; Correa-Baena, J.-P.; Grätzel, M.; Hagfeldt, A.; Abate, A. Perovskite Solar Cells: From the Atomic Level to Film Quality and Device Performance. *Angew. Chem., Int. Ed.* **2018**, *57*, 2554−2569.

(4) Yin, W.-J.; Shi, T.; Yan, Y. Superior Photovoltaic Properties of Lead Halide Perovskites: Insights from First-Principles Theory. *J. Phys. Chem. C* **2015**, *119*, 5253−5264.

(5) Herz, L. M. Charge-Carrier Mobilities in Metal Halide Perovskites: Fundamental Mechanisms and Limits. *ACS Energy Lett.* **2017**, *2*, 1539−1548.

(6) Even, J.; Pedesseau, L.; Katan, C. Analysis of Multivalley and Multibandgap Absorption and Enhancement of Free Carriers Related to Exciton Screening in Hybrid Perovskites. *J. Phys. Chem. C* **2014**, *118*, 11566−11572.

(7) Yang, Y.; Ostrowski, D. P.; France, R. M.; Zhu, K.; van de Lagemaat, J.; Luther, J. M.; Beard, M. C. Observation of a Hot-Phonon Bottleneck in Lead-Iodide Perovskites. *Nat. Photonics* **2016**, *10*, 53−59.

(8) Miyata, A.; Mitioglu, A.; Plochocka, P.; Portugall, O.; Wang, J. T.-W.; Stranks, S. D.; Snaith, H. J.; Nicholas, R. J. Direct Measurement of the Exciton Binding Energy and Effective Masses for Charge Carriers in Organic-Inorganic Tri-Halide Perovskites. *Nat. Phys.* **2015**, *11*, 582−587.

(9) Herz, L. M. Charge-Carrier Dynamics in Organic-Inorganic Metal Halide Perovskites. *Annu. Rev. Phys. Chem.* **2016**, *67*, 65−89.

(10) Umari, P.; Mosconi, E.; De Angelis, F. Infrared Dielectric Screening Determines the Low Exciton Binding Energy of Metal-Halide Perovskites. *J. Phys. Chem. Lett.* **2018**, *9*, 620−627.

(11) Yang, Z.; Surrente, A.; Galkowski, K.; Bruyant, N.; Maude, D. K.; Haghighirad, A. A.; Snaith, H. J.; Plochocka, P.; Nicholas, R. J. Unraveling the Exciton Binding Energy and the Dielectric Constant in Single-Crystal Methylammonium Lead Triiodide Perovskite. *J. Phys. Chem. Lett.* **2017**, *8*, 1851−1855.

(12) Jha, A.; Duan, H.-G.; Tiwari, V.; Nayak, P. K.; Snaith, H. J.; Thorwart, M.; Miller, R. J. D. Direct Observation of Ultrafast Exciton Dissociation in Lead Iodide Perovskite by 2D Electronic Spectroscopy. *ACS Photonics* **2018**, *5*, 852−860.

(13) D'Innocenzo, V.; Grancini, G.; Alcocer, M. J. P.; Kandada, A. R. S.; Stranks, S. D.; Lee, M. M.; Lanzani, G.; Snaith, H. J.; Petrozza, A. Excitons Versus Free Charges in Organo-Lead Tri-Halide Perovskites. *Nat. Commun.* **2014**, *5*, 3586.

(14) Dong, Q.; Fang, Y.; Shao, Y.; Mulligan, P.; Qiu, J.; Cao, L.; Huang, J. Electron-Hole Diffusion Lengths > 175 μm in Solution-Grown $CH_3NH_3PbI_3$ Single Crystals. *Science* **2015**, *347*, 967−970.

(15) Johnston, M. B.; Herz, L. M. Hybrid Perovskites for Photovoltaics: Charge-Carrier Recombination, Diffusion, and Radiative Efficiencies. *Acc. Chem. Res.* **2016**, *49*, 146−154.

(16) Luo, J.; Wang, X.; Li, S.; Liu, J.; Guo, Y.; Niu, G.; Yao, L.; Fu, Y.; Gao, L.; Dong, Q.; et al. Efficient and Stable Emission of Warm-White Light from Lead-Free Halide Double Perovskites. *Nature* **2018**, *563*, 541−545.

(17) Wang, X.; Meng, W.; Liao, W.; Wang, J.; Xiong, R.-G.; Yan, Y. Atomistic Mechanism of Broadband Emission in Metal Halide Perovskites. *J. Phys. Chem. Lett.* **2019**, *10*, 501−506.

(18) Park, M.; Neukirch, A. J.; Reyes-Lillo, S. E.; Lai, M.; Ellis, S. R.; Dietze, D.; Neaton, J. B.; Yang, P.; Tretiak, S.; Mathies, R. A. Excited-State Vibrational Dynamics toward the Polaron in Methylammonium Lead Iodide Perovskite. *Nat. Commun.* **2018**, *9*, 2525.

(19) Batignani, G.; Fumero, G.; Srimath Kandada, A. R.; Cerullo, G.; Gandini, M.; Ferrante, C.; Petrozza, A.; Scopigno, T. Probing Femtosecond Lattice Displacement Upon Photo-Carrier Generation in Lead Halide Perovskite. *Nat. Commun.* **2018**, *9*, 1971.

(20) Ivanovska, T.; Dionigi, C.; Mosconi, E.; De Angelis, F.; Liscio, F.; Morandi, V.; Ruani, G. Long-Lived Photoinduced Polarons in Organohalide Perovskites. *J. Phys. Chem. Lett.* **2017**, *8*, 3081−3086.

(21) Smith, M. D.; Karunadasa, H. I. White-Light Emission from Layered Halide Perovskites. *Acc. Chem. Res.* **2018**, *51*, 619−627.

(22) Miyata, K.; Meggiolaro, D.; Trinh, M. T.; Joshi, P. P.; Mosconi, E.; Jones, S. C.; De Angelis, F.; Zhu, X. Y. Large Polarons in Lead Halide Perovskites. *Sci. Adv.* **2017**, *3*, No. e1701217.

(23) Zhu, X. Y.; Podzorov, V. Charge Carriers in Hybrid Organic−Inorganic Lead Halide Perovskites Might Be Protected as Large Polarons. *J. Phys. Chem. Lett.* **2015**, *6*, 4758−4761.

(24) Chen, Y.; Yi, H. T.; Wu, X.; Haroldson, R.; Gartstein, Y. N.; Rodionov, Y. I.; Tikhonov, K. S.; Zakhidov, A.; Zhu, X. Y.; Podzorov, V. Extended Carrier Lifetimes and Diffusion in Hybrid Perovskites Revealed by Hall Effect and Photoconductivity Measurements. *Nat. Commun.* **2016**, *7*, 12253.

(25) Bretschneider, S. A.; Ivanov, I.; Wang, H. I.; Miyata, K.; Zhu, X.; Bonn, M. Quantifying Polaron Formation and Charge Carrier Cooling in Lead-Iodide Perovskites. *Adv. Mater.* **2018**, *30*, 1707312.

(26) Ambrosio, F.; Wiktor, J.; De Angelis, F.; Pasquarello, A. Origin of Low Electron−Hole Recombination Rate in Metal Halide Perovskites. *Energy Environ. Sci.* **2018**, *11*, 101−105.

(27) Fabini, D. H.; Siaw, T. A.; Stoumpos, C. C.; Laurita, G.; Olds, D.; Page, K.; Hu, J. G.; Kanatzidis, M. G.; Han, S.; Seshadri, R. Universal Dynamics of Molecular Reorientation in Hybrid Lead Iodide Perovskites. *J. Am. Chem. Soc.* **2017**, *139*, 16875−16884.

(28) Zheng, K.; Abdellah, M.; Zhu, Q.; Kong, Q.; Jennings, G.; Kurtz, C. A.; Messing, M. E.; Niu, Y.; Gosztola, D. J.; Al-Marri, M. J.; et al. Direct Experimental Evidence for Photoinduced Strong-Coupling Polarons in Organolead Halide Perovskite Nanoparticles. *J. Phys. Chem. Lett.* **2016**, *7*, 4535−4539.

(29) Nie, W.; Blancon, J.-C.; Neukirch, A. J.; Appavoo, K.; Tsai, H.; Chhowalla, M.; Alam, M. A.; Sfeir, M. Y.; Katan, C.; Even, J.; et al. Light-Activated Photocurrent Degradation and Self-Healing in Perovskite Solar Cells. *Nat. Commun.* **2016**, *7*, 11574.

(30) Neukirch, A. J.; Nie, W.; Blancon, J.-C.; Appavoo, K.; Tsai, H.; Sfeir, M. Y.; Katan, C.; Pedesseau, L.; Even, J.; Crochet, J. J.; et al. Polaron Stabilization by Cooperative Lattice Distortion and Cation Rotations in Hybrid Perovskite Materials. *Nano Lett.* **2016**, *16*, 3809−3816.

(31) Straus, D. B.; Hurtado Parra, S.; Iotov, N.; Gebhardt, J.; Rappe, A. M.; Subotnik, J. E.; Kikkawa, J. M.; Kagan, C. R. Direct

Observation of Electron−Phonon Coupling and Slow Vibrational Relaxation in Organic−Inorganic Hybrid Perovskites. *J. Am. Chem. Soc.* **2016**, *138*, 13798−13801.
(32) Shao, Y.; Fang, Y.; Li, T.; Wang, Q.; Dong, Q.; Deng, Y.; Yuan, Y.; Wei, H.; Wang, M.; Gruverman, A.; et al. Grain Boundary Dominated Ion Migration in Polycrystalline Organic−Inorganic Halide Perovskite Films. *Energy Environ. Sci.* **2016**, *9*, 1752−1759.
(33) Galisteo-López, J. F.; Li, Y.; Míguez, H. Three-Dimensional Optical Tomography and Correlated Elemental Analysis of Hybrid Perovskite Microstructures: An Insight into Defect-Related Lattice Distortion and Photoinduced Ion Migration. *J. Phys. Chem. Lett.* **2016**, *7*, 5227−5234.
(34) Wang, Y.; Sumpter, B. G.; Huang, J.; Zhang, H.; Liu, P.; Yang, H.; Zhao, H. Density Functional Studies of Stoichiometric Surfaces of Orthorhombic Hybrid Perovskite $CH_3NH_3PbI_3$. *J. Phys. Chem. C* **2015**, *119*, 1136−1145.
(35) Haruyama, J.; Sodeyama, K.; Han, L.; Tateyama, Y. Termination Dependence of Tetragonal $CH_3NH_3PbI_3$ Surfaces for Perovskite Solar Cells. *J. Phys. Chem. Lett.* **2014**, *5*, 2903−2909.
(36) Lee, Y. M.; Park, J.; Yu, B. D.; Hong, S.; Jung, M.-C.; Nakamura, M. Surface Instability of Sn-Based Hybrid Perovskite Thin Film, $CH_3NH_3SnI_3$: The Origin of Its Material Instability. *J. Phys. Chem. Lett.* **2018**, *9*, 2293−2297.
(37) Quarti, C.; De Angelis, F.; Beljonne, D. Influence of Surface Termination on the Energy Level Alignment at the $CH_3NH_3PbI_3$ Perovskite/C60 Interface. *Chem. Mater.* **2017**, *29*, 958−968.
(38) Zhang, L.; Ju, M.-G.; Liang, W. The Effect of Moisture on the Structures and Properties of Lead Halide Perovskites: A First-Principles Theoretical Investigation. *Phys. Chem. Chem. Phys.* **2016**, *18*, 23174−23183.
(39) Wang, W.-W.; Dang, J.-S.; Jono, R.; Segawa, H.; Sugimoto, M. A First-Principles Prediction on the "Healing Effect" of Graphene Preventing Carrier Trapping near the Surface of Metal Halide Perovskites. *Chem. Sci.* **2018**, *9*, 3341−3353.
(40) Mosconi, E.; Azpiroz, J. M.; De Angelis, F. Ab Initio Molecular Dynamics Simulations of Methylammonium Lead Iodide Perovskite Degradation by Water. *Chem. Mater.* **2015**, *27*, 4885−4892.
(41) Zhang, L.; Sit, P. H. L. Ab Initio Study of the Role of Oxygen and Excess Electrons in the Degradation of $CH_3NH_3PbI_3$. *J. Mater. Chem. A* **2017**, *5*, 9042−9049.
(42) Zhang, L.; Sit, P. H. L. Ab Initio Study of Interaction of Water, Hydroxyl Radicals, and Hydroxide Ions with $CH_3NH_3PbI_3$ and $CH_3NH_3PbBr_3$ Surfaces. *J. Phys. Chem. C* **2015**, *119*, 22370−22378.
(43) Hao, W.; Chen, X.; Li, S. Synergistic Effects of Water and Oxygen Molecule Co-Adsorption on (001) Surfaces of Tetragonal $CH_3NH_3PbI_3$: A First-Principles Study. *J. Phys. Chem. C* **2016**, *120*, 28448−28455.
(44) Tong, C.-J.; Geng, W.; Tang, Z.-K.; Yam, C.-Y.; Fan, X.-L.; Liu, J.; Lau, W.-M.; Liu, L.-M. Uncovering the Veil of the Degradation in Perovskite $CH_3NH_3PbI_3$ Upon Humidity Exposure: A First-Principles Study. *J. Phys. Chem. Lett.* **2015**, *6*, 3289−3295.
(45) Koocher, N. Z.; Saldana-Greco, D.; Wang, F.; Liu, S.; Rappe, A. M. Polarization Dependence of Water Adsorption to $CH_3NH_3PbI_3$ (001) Surfaces. *J. Phys. Chem. Lett.* **2015**, *6*, 4371−4378.
(46) Ohmann, R.; Ono, L. K.; Kim, H.-S.; Lin, H.; Lee, M. V.; Li, Y.; Park, N.-G.; Qi, Y. Real-Space Imaging of the Atomic Structure of Organic−Inorganic Perovskite. *J. Am. Chem. Soc.* **2015**, *137*, 16049−16054.
(47) She, L.; Liu, M.; Zhong, D. Atomic Structures of $CH_3NH_3PbI_3$ (001) Surfaces. *ACS Nano* **2016**, *10*, 1126−1131.
(48) Murali, B.; Dey, S.; Abdelhady, A. L.; Peng, W.; Alarousu, E.; Kirmani, A. R.; Cho, N.; Sarmah, S. P.; Parida, M. R.; Saidaminov, M. I.; et al. Surface Restructuring of Hybrid Perovskite Crystals. *ACS Energy Lett.* **2016**, *1*, 1119−1126.
(49) Tsai, H.; Asadpour, R.; Blancon, J.-C.; Stoumpos, C. C.; Durand, O.; Strzalka, J. W.; Chen, B.; Verduzco, R.; Ajayan, P. M.; Tretiak, S.; et al. Light-Induced Lattice Expansion Leads to High-Efficiency Perovskite Solar Cells. *Science* **2018**, *360*, 67−70.
(50) Yin, J.; Cortecchia, D.; Krishna, A.; Chen, S.; Mathews, N.; Grimsdale, A. C.; Soci, C. Interfacial Charge Transfer Anisotropy in Polycrystalline Lead Iodide Perovskite Films. *J. Phys. Chem. Lett.* **2015**, *6*, 1396−1402.
(51) Baikie, T.; Fang, Y.; Kadro, J. M.; Schreyer, M.; Wei, F.; Mhaisalkar, S. G.; Graetzel, M.; White, T. J. Synthesis and Crystal Chemistry of the Hybrid Perovskite $(CH_3NH_3)PbI_3$ for Solid-State Sensitised Solar Cell Applications. *J. Mater. Chem. A* **2013**, *1*, 5628−5641.
(52) Poglitsch, A.; Weber, D. Dynamic Disorder in Methylammoniumtrihalogenoplumbates (II) Observed by Millimeter-Wave Spectroscopy. *J. Chem. Phys.* **1987**, *87*, 6373−6378.
(53) Quarti, C.; Mosconi, E.; De Angelis, F. Interplay of Orientational Order and Electronic Structure in Methylammonium Lead Iodide: Implications for Solar Cell Operation. *Chem. Mater.* **2014**, *26*, 6557−6569.
(54) Kresse, G.; Furthmüller, J. Efficient Iterative Schemes for Ab Initio Total-Energy Calculations Using a Plane-Wave Basis Set. *Phys. Rev. B: Condens. Matter Mater. Phys.* **1996**, *54*, 11169−11186.
(55) Blöchl, P. E. Projector Augmented-Wave Method. *Phys. Rev. B: Condens. Matter Mater. Phys.* **1994**, *50*, 17953−17979.
(56) Perdew, J. P.; Burke, K.; Ernzerhof, M. Generalized Gradient Approximation Made Simple. *Phys. Rev. Lett.* **1996**, *77*, 3865−3868.
(57) Grimme, S. Semiempirical GGA-Type Density Functional Constructed with a Long-Range Dispersion Correction. *J. Comput. Chem.* **2006**, *27*, 1787−1799.
(58) Zhang, X.; Lu, G. Subspace Formulation of Time-Dependent Density Functional Theory for Large-Scale Calculations. *J. Chem. Phys.* **2015**, *143*, No. 064110.
(59) Umari, P.; Mosconi, E.; De Angelis, F. Relativistic GW Calculations on $CH_3NH_3PbI_3$ and $CH_3NH_3SnI_3$ Perovskites for Solar Cell Applications. *Sci. Rep.* **2014**, *4*, 4467.
(60) Du, M.-H. Density Functional Calculations of Native Defects in $CH_3NH_3PbI_3$: Effects of Spin−Orbit Coupling and Self-Interaction Error. *J. Phys. Chem. Lett.* **2015**, *6*, 1461−1466.
(61) Brivio, F.; Butler, K. T.; Walsh, A.; van Schilfgaarde, M. Relativistic Quasiparticle Self-Consistent Electronic Structure of Hybrid Halide Perovskite Photovoltaic Absorbers. *Phys. Rev. B: Condens. Matter Mater. Phys.* **2014**, *89*, 155204.
(62) Refaely-Abramson, S.; Jain, M.; Sharifzadeh, S.; Neaton, J. B.; Kronik, L. Solid-State Optical Absorption from Optimally Tuned Time-Dependent Range-Separated Hybrid Density Functional Theory. *Phys. Rev. B: Condens. Matter Mater. Phys.* **2015**, *92*, No. 081204(R).
(63) Nan, G.; Zhang, X.; Abdi-Jalebi, M.; Andaji-Garmaroudi, Z.; Stranks, S. D.; Lu, G.; Beljonne, D. How Methylammonium Cations and Chlorine Dopants Heal Defects in Lead Iodide Perovskites. *Adv. Energy Mater.* **2018**, *8*, 1702754.
(64) Nan, G.; Zhang, X.; Lu, G. Self-Healing of Photocurrent Degradation in Perovskite Solar Cells: The Role of Defect-Trapped Excitons. *J. Phys. Chem. Lett.* **2019**, *10*, 7774−7780.
(65) Huang, L.-Y.; Zhang, X.; Zhang, M.; Lu, G. Effect of Point Defects on Optical Properties of Graphene Fluoride: A First-Principles Study. *J. Phys. Chem. C* **2017**, *121*, 12855−12862.
(66) Lee, J.-H.; Bristowe, N. C.; Bristowe, P. D.; Cheetham, A. K. Role of Hydrogen-Bonding and Its Interplay with Octahedral Tilting in $CH_3NH_3PbI_3$. *Chem. Commun.* **2015**, *51*, 6434−6437.
(67) Wendler, K.; Thar, J.; Zahn, S.; Kirchner, B. Estimating the Hydrogen Bond Energy. *J. Phys. Chem. A* **2010**, *114*, 9529−9536.
(68) Murali, B.; Yengel, E.; Yang, C.; Peng, W.; Alarousu, E.; Bakr, O. M.; Mohammed, O. F. The Surface of Hybrid Perovskite Crystals: A Boon or Bane. *ACS Energy Lett.* **2017**, *2*, 846−856.
(69) Kubicki, D. J.; Prochowicz, D.; Hofstetter, A.; Péchy, P.; Zakeeruddin, S. M.; Grätzel, M.; Emsley, L. Cation Dynamics in Mixed-Cation $(MA)_X(FA)_{1-X}PbI_3$ Hybrid Perovskites from Solid-State NMR. *J. Am. Chem. Soc.* **2017**, *139*, 10055−10061.
(70) Stroppa, A.; Quarti, C.; De Angelis, F.; Picozzi, S. Ferroelectric Polarization of $CH_3NH_3PbI_3$: A Detailed Study Based on Density

https://dx.doi.org/10.1021/acs.jpclett.0c00673
J. Phys. Chem. Lett. 2020, 11, 2983−2991

Functional Theory and Symmetry Mode Analysis. *J. Phys. Chem. Lett.* **2015**, *6*, 2223−2231.
(71) Park, B.-w.; Kedem, N.; Kulbak, M.; Lee, D. Y.; Yang, W. S.; Jeon, N. J.; Seo, J.; Kim, G.; Kim, K. J.; Shin, T. J.; et al. Understanding How Excess Lead Iodide Precursor Improves Halide Perovskite Solar Cell Performance. *Nat. Commun.* **2018**, *9*, 3301.
(72) Bi, D.; Tress, W.; Dar, M. I.; Gao, P.; Luo, J.; Renevier, C.; Schenk, K.; Abate, A.; Giordano, F.; Correa Baena, J.-P.; et al. Efficient Luminescent Solar Cells Based on Tailored Mixed-Cation Perovskites. *Sci. Adv.* **2016**, *2*, No. e1501170.
(73) Roldán-Carmona, C.; Gratia, P.; Zimmermann, I.; Grancini, G.; Gao, P.; Graetzel, M.; Nazeeruddin, M. K. High Efficient Methylammonium Lead Triiodide Perovskite Solar Cells: The Relevance of Non-Stoichiometric Precursors. *Energy Environ. Sci.* **2015**, *8*, 3550−3556.
(74) Iaru, C. M.; Geuchies, J. J.; Koenraad, P. M.; Vanmaekelbergh, D.; Silov, A. Y. Strong Carrier−Phonon Coupling in Lead Halide Perovskite Nanocrystals. *ACS Nano* **2017**, *11*, 11024−11030.
(75) Ma, X.; Pan, F.; Li, H.; Shen, P.; Ma, C.; Zhang, L.; Niu, H.; Zhu, Y.; Xu, S.; Ye, H. Mechanism of Single-Photon Upconversion Photoluminescence in All-Inorganic Perovskite Nanocrystals: The Role of Self-Trapped Excitons. *J. Phys. Chem. Lett.* **2019**, *10*, 5989−5996.
(76) Lao, X.; Yang, Z.; Su, Z.; Bao, Y.; Zhang, J.; Wang, X.; Cui, X.; Wang, M.; Yao, X.; Xu, S. Anomalous Temperature-Dependent Exciton−Phonon Coupling in Cesium Lead Bromide Perovskite Nanosheets. *J. Phys. Chem. C* **2019**, *123*, 5128−5135.
(77) Imran, M.; Di Stasio, F.; Dang, Z.; Canale, C.; Khan, A. H.; Shamsi, J.; Brescia, R.; Prato, M.; Manna, L. Colloidal Synthesis of Strongly Fluorescent $CsPbBr_3$ Nanowires with Width Tunable Down to the Quantum Confinement Regime. *Chem. Mater.* **2016**, *28*, 6450−6454.
(78) Protesescu, L.; Yakunin, S.; Bodnarchuk, M. I.; Krieg, F.; Caputo, R.; Hendon, C. H.; Yang, R. X.; Walsh, A.; Kovalenko, M. V. Nanocrystals of Cesium Lead Halide Perovskites ($CsPbX_3$, X = Cl, Br, and I): Novel Optoelectronic Materials Showing Bright Emission with Wide Color Gamut. *Nano Lett.* **2015**, *15*, 3692−3696.
(79) Bekenstein, Y.; Koscher, B. A.; Eaton, S. W.; Yang, P.; Alivisatos, A. P. Highly Luminescent Colloidal Nanoplates of Perovskite Cesium Lead Halide and Their Oriented Assemblies. *J. Am. Chem. Soc.* **2015**, *137*, 16008−16011.
(80) Swarnkar, A.; Marshall, A. R.; Sanehira, E. M.; Chernomordik, B. D.; Moore, D. T.; Christians, J. A.; Chakrabarti, T.; Luther, J. M. Quantum Dot−Induced Phase Stabilization of α-$CsPbI_3$ Perovskite for High-Efficiency Photovoltaics. *Science* **2016**, *354*, 92−95.
(81) Mahata, A.; Meggiolaro, D.; De Angelis, F. From Large to Small Polarons in Lead, Tin, and Mixed Lead-Tin Halide Perovskites. *J. Phys. Chem. Lett.* **2019**, *10*, 1790−1798.
(82) Gao, Y.; Zhang, M.; Zhang, X.; Lu, G. Decreasing Exciton Binding Energy in Two-Dimensional Halide Perovskites by Lead Vacancies. *J. Phys. Chem. Lett.* **2019**, *10*, 3820−3827.
(83) Qin, C.; Matsushima, T.; Fujihara, T.; Potscavage, W. J., Jr.; Adachi, C. Degradation Mechanisms of Solution-Processed Planar Perovskite Solar Cells: Thermally Stimulated Current Measurement for Analysis of Carrier Traps. *Adv. Mater.* **2016**, *28*, 466−471.

https://dx.doi.org/10.1021/acs.jpclett.0c00673
J. Phys. Chem. Lett. 2020, 11, 2983−2991